Available online at www.sciencedirect.com

ScienceDirect

Procedia Computer Science 96 (2016) 930 – 938

Procedia Computer Science

20th International Conference on Knowledge Based and Intelligent Information and Engineering Systems, KES2016, 5-7 September 2016, York, United Kingdom

Numerical modeling of non-destructive testing of composites

Igor Petrov[a], Alexey Vasyukov[a], Katerina Beklemysheva[a*], Alexey Ermakov[a], Alena Favorskaya[a]

[a]*Moscow Institute of Physics and Technology, 9 Intitutsky per., Dolgoprudniy, 141700 Russian Federation*

Abstract

Low-velocity strikes are considered as one of the most dangerous load types for composites, especially in aviation. They do not lead to an immediate destruction of a whole detail, but inner damage, provoking a delamination between layers or between fiber and matrix, lowers the material strength and may cause a destruction during the flight. This inner damage can only be noticed via complex study, which increases an exploitation cost. Numerical modeling can help to interpret the results obtained from common portable devices, which are currently used for metals. The modification of known methodology can be reliably used for composites. In this research, a hybrid grid-characteristic method of 1-2 order on irregular tetrahedral grid is used. A carbon fiber polymer matrix of unidirectional composite is modeled as a homogeneous orthotropic media with a single distinguished direction along the fiber. As a result, the one-dimensional graphics, which correspond to A-scans in real devices, were obtained. The detailed analysis of received data confirms a rationality of proposed methodoly.

Peer-review under responsibility of KES International

Keywords: numerical modelling; grid-characteristic method; composites; composites destruction; non-destructive testing

* Corresponding author. *E-mail address:* amisto@yandex.ru

1. Introduction

Modern technology utilizes the composites in a great variety of ways, including bearing structures, which require the endurance under static, dynamic, and fatigue loadings. Composites have low weight and high strength in comparison with traditional construction materials, and that make them extremely useful, for example, in aviation. However, the certain problems were exposed during their exploitation, including the complexity of ultrasonic Non-Destructive Testing (NDT)[1,2,3,4,5,6,7]. Portable devices that are currently used for a non-destructive testing are designed for isotropic homogenous materials and use ray method, which does not consider the interconversion of

Peer-review under responsibility of KES International
doi:10.1016/j.procs.2016.08.272

wave types[8]. They are not effective for composites, which are heterogeneous, anisotropic and has specific inner damage types that are not so dangerous for metals[9,10].

One of the most dangerous inner damage types is a delamination between layers and between fiber and matrix[11,12,13]. It do not lead to an immediate destruction of a whole detail, but unpredictably lowers material strength and may cause a destruction during exploitation, e. g., in aviation during the flight. This damage type can appear due to low-velocity strikes: exposure to weather, maintenance, and transportation failures[14]. It only can be noticed via complex study, which cannot be conducted outside the laboratory[15]. While dangerous for the whole construction damages can be observed with the naked eye for metals, it is much harder for composites. The requirement of laboratory study increases the exploitation cost and lowers the usability of composites in mass production. Numerical modeling can help to interpret the results obtained from common portable devices, which are currently used for metals. The modification of this methodology can be reliably used for composites.

The current research is dedicated to the numerical modeling of the problem via a hybrid grid-characteristic method of 1-2 order on irregular tetrahedral grid[16,17,18]. This method is based on the characteristic properties of the elastic deformable solids as a set of equations and models accurately propagation, reflection, and refraction of wavefronts, including their interconversion on different border and contact types. The method was verified on various problem statements by comparison with experiments in different science fields, including seismology[19,20], materials science[14,21,22], and biomechanics[18,23]. A carbon fiber polymer matrix unidirectional composite is modeled as orthotropic media with a single distinguished direction along the fiber[24].

The remainder of this paper is organized as follows. Section 2 describes the material models and the numerical method. Problem statement is presented in Section 3. The obtained wavefronts and their analysis are presented in Section 4. The analysis of A-scans (one-dimensional graphics, which represent a time dependence of receiving signal) for steel and composite monolayer is presented in Section 5 and Section 6, respectively. Section 7 includes the conclusions.

2. Mathematical model and numerical method

Two materials are used in this research. The first one is steel and it is modeled as isotropic elastic deformable solid, $\rho = 7800$ kg/m^3, $\lambda = 99.43$ GPa, $\mu = 78.13$ GPa (ρ – material density, λ and μ – Lame parameters). The second one is a composite monolayer – carbon fiber with unidirectional laying and epoxy matrix – and is modeled as a homogenous orthotropic elastic deformable solid with a single distinguished direction along the fiber, E_{11}^{+}= 16483 MPa, $E_{11}^{-} = 13376$ MPa, $E_{22}^{+} = 805$ MPa, $E_{22}^{-} = 854$ MPa, $G_{12} = 437$ MPa, $\rho = 1580$ kg/m^3, $\nu = 0.32$. E_{11}^{+} is Young's modulus along the fiber laying, tensile load; E_{11}^{-} is Young's modulus along the fiber laying, compression load; E_{22}^{+} is Young's modulus across the fiber laying, tensile load; E_{22}^{-} is Young's modulus across the fiber laying, compression load, G_{12} is a shear modulus, ρ – density, ν is a Poisson modulus.

The closed system of equations for deformable solid consists of motion equations, rheological correlations, and the equation of state:

$$\rho \dot{v}_i = \nabla_j \sigma_{ij} + f_i \quad ,$$

$$\dot{\sigma}_{ij} = q_{ijkl}\, \dot{\varepsilon}_{kl} + F_{ij} \tag{1}$$

where ρ is a density, v_i is a displacement speed components, ∇_j is a covariant derivative by j coordinate, σ_{ij} is a stress tensor, ε_{ij} is a strain tensor, f_i is a mass forces, F_{ij} is the right part, depending on a rheology model, q_{ijkl} is the fourth order tensor also depending on a rheology model. The system can be rewritten as follows:

$$\frac{\partial \boldsymbol{u}}{\partial t} + \boldsymbol{A}_x \frac{\partial \boldsymbol{u}}{\partial x} + \boldsymbol{A}_y \frac{\partial \boldsymbol{u}}{\partial y} + \boldsymbol{A}_z \frac{\partial \boldsymbol{u}}{\partial z} = \boldsymbol{f} \,, \tag{2}$$

where $\boldsymbol{u} = \left\{ v_x, v_y, v_z, \sigma_{xx}, \sigma_{yy}, \sigma_{zz}, \sigma_{xy}, \sigma_{xz}, \sigma_{yz} \right\}^T$ is a vector of unknown functions, x, y, z are independent spatial variables, t is a time, $\boldsymbol{f}$ is the right parts vector. The exact form of matrices **A** for isotropic and anisotropic models can be found in[17] and[24], respectively.

It is required to solve the set of equations the hybrid grid-characteristic method of 1-2 order on irregular tetrahedral grid[16,17,18]. This method is based on the characteristic properties of the elastic deformable solids set of equations into account and models accurately propagation, reflection, and refraction of wavefronts, including their interconversion on different border and contact types. The proposed method was verified in various science fields [18,19,20,21,22,23].

3. Problem statement

In the main calculation series the 70 mm × 70 mm × 10 mm plate is considered. A rectangular notch is situated in the middle of the backside (Fig. 1, b)), its dimensions are 10 mm × 10 mm × 3.75 mm. The characteristic grid step is 0.125 mm, the time step is calculated from the Courant condition. Several calculations were also performed to illustrate the elastic wave's behavior during interaction with open and close fractures.

The source of the diagnostic impulse (striker, piezoelectric crystal) is modeled by equivalent impulse (velocity 100 m/s along the OZ axis during the first time step) in the 2.2 mm × 2.2 mm area in the middle of the front side. The receiver is modeled by obtaining the averaged signal on the same size area. Two types of receiver are considered. The first one coincides with the source; the second one is adjacent to the source by the *y* coordinate. The first case corresponds with a combined sensor (emitter and receiver are the same piezoelectric crystal), the second case deals with a separated-combined sensor (emitter and receiver are different piezoelectric crystals placed close to each other), Fig. 1, a).

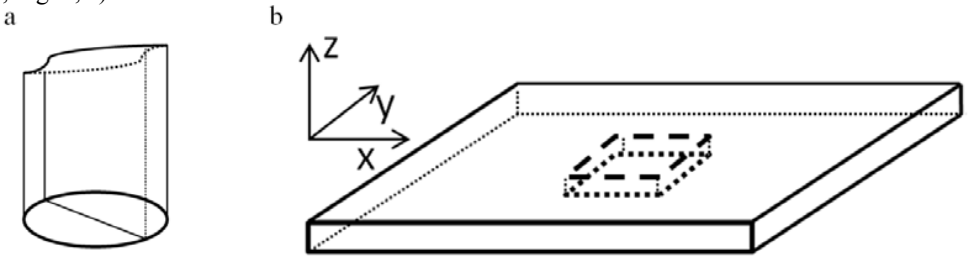

Fig. 1. (a) separated-combined sensor; (b) general view of geometry.

Table 1. Varied parameters.

Calculation number	1	2	3	4	5
Notch depth, mm	0.000	1.875	3.750	5.625	7.500
Distance from plate center to the sensor by x axis, mm	0.0	2.5	5.0	7.5	10.0
Diagnostic impulse length, s	0.0007	0.0021	0.0035	0.0049	0.0063
Sensor size, mm	0.6	1.2	2.2	3.2	4.2

Different modeling variations were considered, and the receiving signals were compared. Five calculations were implemented for each of the parameters and both of the considered materials – steel and composite. When one of the parameters was varied, others parameters were locked (Table 1).

4. Wavefronts analysis

One of the NDT problems is to determine a location of inner damage areas like fractures and delaminations. An open fracture has two free borders and behaves like a usual free border, when an elastic wave falls on it. A closed fracture has the contacting edges. When a compression wave passes through, tensile wave reflects. The behavior of a shear wave depends on friction forces.

Primarily, we look at P-waves, which are the easiest to generate. So called P-wave with relatively high amplitude appears after a simple normal strike on the surface. In this case, it has two main components – a compression wave in front and a tensile wave behind. Also a surface wave (Rayleigh wave) can be observed, but it propagates along the

surface and does not interact with the damaged areas. Fig. 2 shows the wave pattern for interaction of P-wave with an open fracture in steel. Thais type of fracture can be easily detected with a P-wave, the reflection does not differ from one with a free border. The signal from the sensor can be recognized by any processing algorithm.

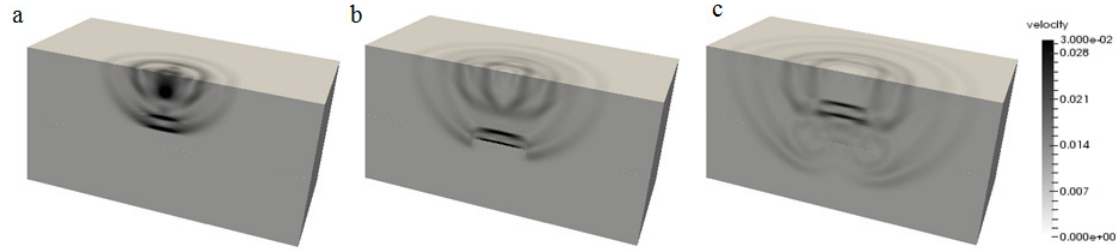

Fig. 2. (a) waves propagation start; (b) fracture interaction; (c) reflected and transmitted waves for interaction of P-wave with an open fracture in steel.

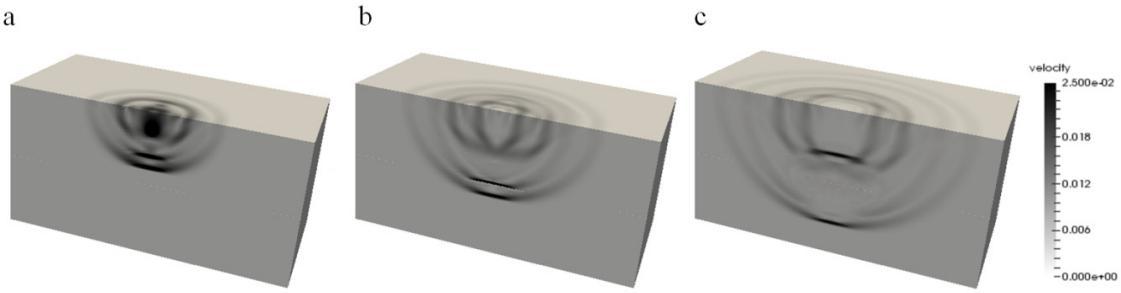

Fig. 3. Interaction of P-wave with a closed fracture in steel:(a) waves propagation start; (b) fracture interaction; (c) reflected and transmitted waves.

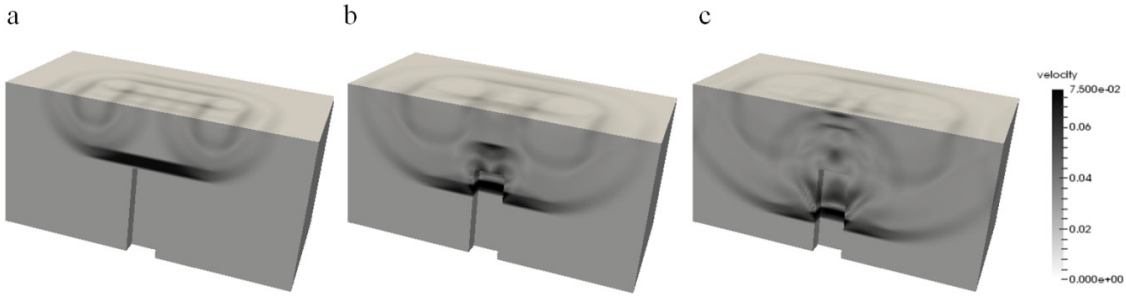

Fig. 4. Interaction of P-wave with a backside notch in steel:(a) waves propagation start; (b) notch interaction; (c) reflected wave.

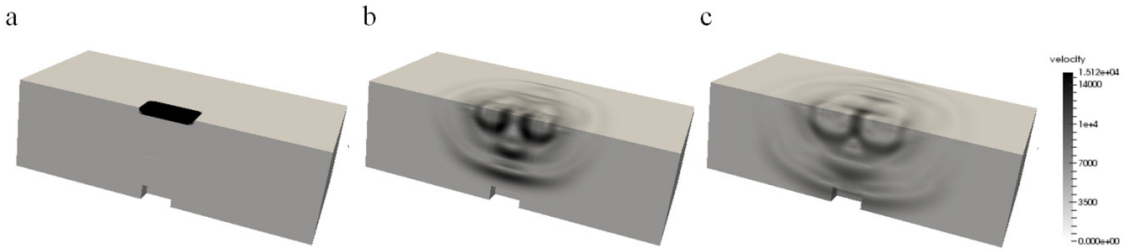

Fig. 5. Interaction of P-wave with a backside notch in a monolayer:(a) waves propagation start; (b) waves propagation; (c) interaction with notch.

Fig. 3 demonstrates the wave pattern for interaction of P-wave with a closed fracture in steel. It can be observed that only a part of impulse, distinguishable by a detector, reflects from the fracture. This peculiarity can lead to different sensor readings, when applying different processing algorithms. Fig. 4 shows the wave pattern for interaction of P-wave with a backside notch in steel. Characteristic patterns in direct and reflected signals can be noticed. Traces of wave fronts interaction with side free borders are also present. Fig. 5 depicts the wave pattern for interaction of P-wave with a backside notch in a composite monolayer. The pattern has quantitative difference with the pattern for a metal plate, because waves propagation is anisotropic and additional shear waves present. A large variety of wave types complicates the sensor data analysis, which will be shown in next sections.

5. Sensor data analysis for a steel plate

The dependencies of signal on the receiver (velocity vector components) with a varying notch depth are depicted in Fig. 6. Graphics of the *z* velocity component show impulse, reflected from the back side. In calculation №1 the plate does not have a notch, and the response time is 0.112 s (160 time steps). With the notch depth being increased, a response time decreases down to 0.028 s (40 time steps): the width of remaining steel between notch bottom and the front side is in four times less than a total plate width. A diagnosing impulse reflects between front and back free borders. This leads to multiple signals registering in the sensor.

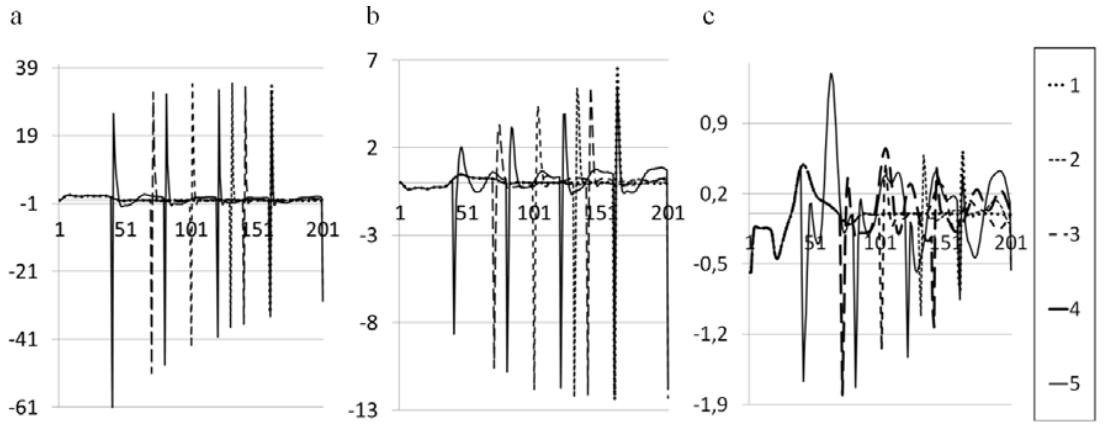

Fig. 6. Sensor data for a varying notch depth:(a) combined sensor, v_z; (b) separated-combined sensor, v_z; (c) separated-combined sensor, v_y. X axis – step number, y axis – velocity, m/s. Different line types correspond with statements from Table 1.

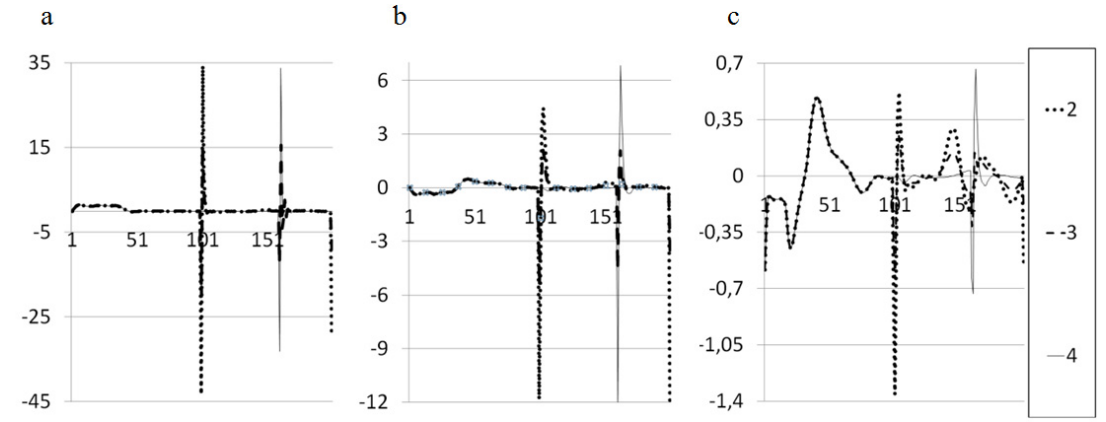

Fig. 7. Sensor data for a varying sensor position:(a) combined sensor, v_z; (b) separated-combined sensor, v_z; (c) separated-combined sensor, v_y. X axis – step number, y axis – velocity, m/s. Different line types correspond with statements from Table 1.

The signal amplitude for a combined sensor v_z is higher than for a separated-combined sensor v_z. The receivers are located on the same *x* coordinate as the emitter, their position is symmetrical, and velocity components are being averaged over the whole receiver area, so velocity components v_x and v_y in a combined sensor and velocity component v_x in a separated-combined sensor are within the calculation error. Velocity component v_y in a separated-combined sensor also shows the dependence of signal on notch depth, but low amplitude and high noise amount make velocity component v_z easier to process and analyze.

Fig. 7 shows the dependency of signal in the receiver (velocity vector components) with a varying sensor position – emitter and receiver are being moved along the OX axis according to values from Table 1. Graphics for statements 1 and 5 are not presented, because they coincide (within the calculation error) with graphics for statements 2 and 4. The graphic for the statement 2 (the sensor is above the notch) shows that the response is coming to the receiver on the 100th time step – similarly to the statement 3 from Fig. 2, which corresponds with a notch depth 3.75 mm. Graphics for the statement 4 (the sensor is outside the notch) show the response on the 160th time step – similarly to the statement 1 from Fig. 2, which corresponds with an intact plate. Graphics for the statement 3 (the sensor is directly above the notch edge) indicate that a part of the direct wave reflects from the back side of the plate, and the other part – from the notch bottom, because the signal shows weaker responses in both of the time steps mentioned. Graphics for the v_y velocity component on a separated-combined sensor (Fig. 6, 7) clearly show the signal from the direct wave, which does not depend on a statement. In Fig. 7, this signal overlaps with the first response for the deepest notch, statement 4.

Fig. 8 shows the dependency of signal in the receiver (velocity vector components) with a varying impulse length according to values from Table 1. With increasing impulse length, the noise amplitude is also increased, and that hinders to the signal processing. Graphics for the v_z velocity component show that at the beginning this component is negative. It explains for of the Rayleigh wave on the previous graphics: with a short impulse length, Rayleigh wave length is less than a grid step in these calculations, and its negative component is indistinguishable.

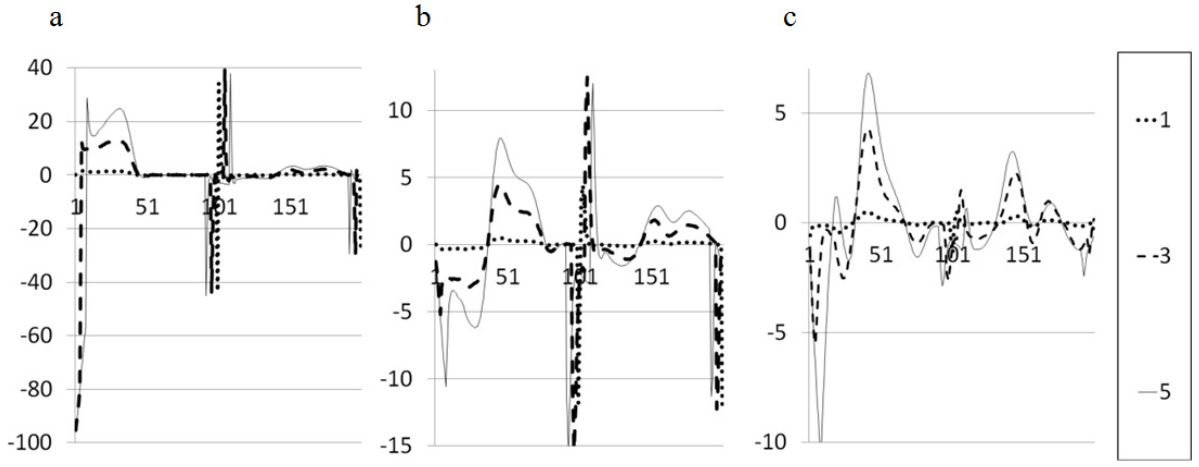

Fig. 8. Sensor data for a varying impulse length:(a) combined sensor, v_z; (b) separated-combined sensor, v_z; (c) separated-combined sensor, v_y. X axis – step number, y axis – velocity, m/s. Different line types correspond with statements from Table 1.

6. Sensor data analysis for a composite monolayer plate

The dependencies of signal in the receiver (velocity vector components) with a varying notch depth according to values from Table 1 are depicted in Fig. 9. The free back border response that comes to the receiver in 350-450 time step in statement 1 has significantly smaller amplitude with respect to the direct impulse than in the corresponding statement for steel. It can result in NDT devices designed for metals ignoring the weak response or giving different values on each measurement. With increasing a notch depth and corresponding decreasing of space between a sensor and a free border the first response comes earlier. The subsequent signal has a high amount of noise. It was possible to distinguish a multiple response due to multiple free border reflection in case of metal, but in case of

anisotropic material the wave pattern from a single strike is much more complex, and diagnosing a multiple response becomes almost impossible. Response amplitude becomes higher with decreasing distance to the free border because spherical wavefront scatters rapidly.

The combined sensor catches the velocity component, perpendicular to the surface. The other components are close to zero. The separated-combined sensor catches the velocity component, perpendicular to the surface, and the velocity component, parallel to the surface and parallel to the sensor orientation. The third component is close to zero. It is caused by the symmetry and averaging over the receiver's area.

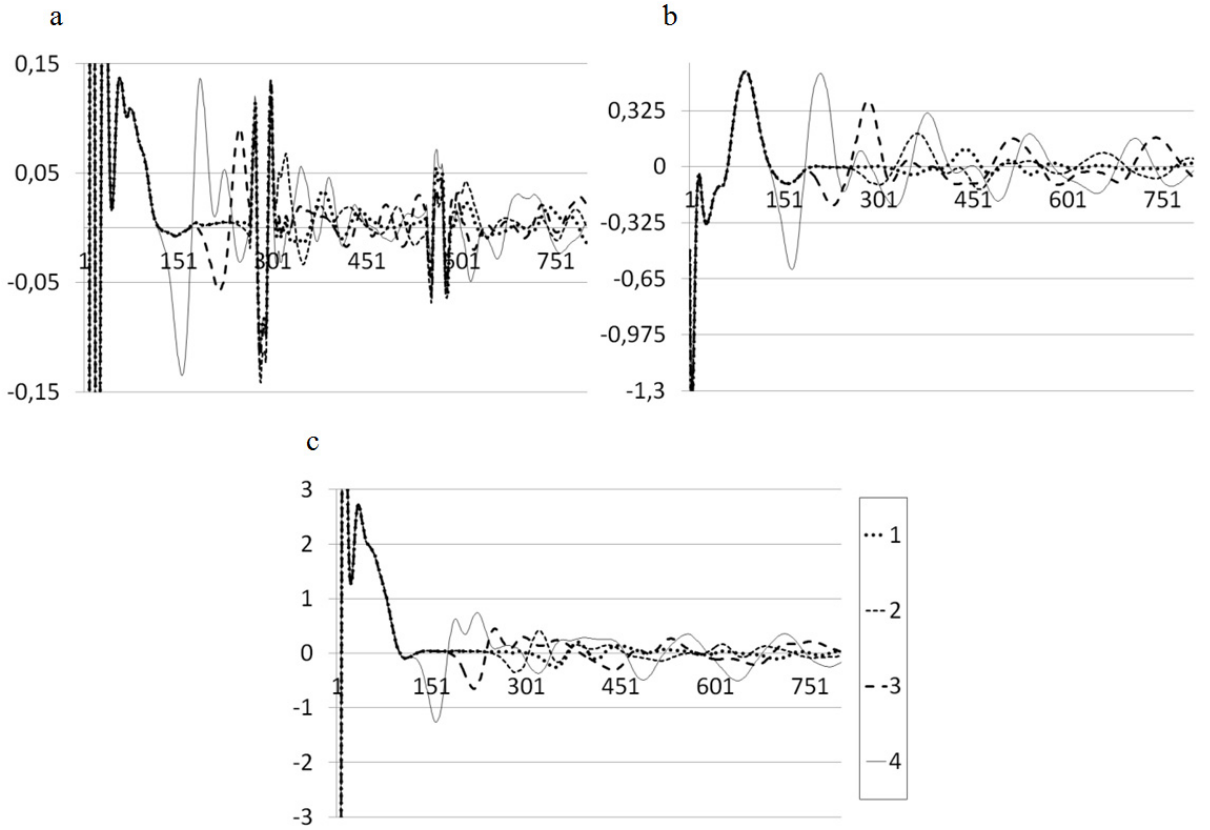

Fig. 9. Sensor data for a varying notch depth:(a) separated-combined sensor, oriented by x axis, v_x; (b) separated-combined sensor, oriented by y axis, v_y; (c) combined sensor, v_z. X axis – step number, y axis – velocity, m/s. Different line types correspond with statements from Table 1.

A stray wave signal can be seen on graphics for OX axis velocity component. Its appearance time step does not depend on notch depth because this wave is a reflection of direct wave from the free border in the OX axis direction, a side of plate. This wave complicates the signal data analysis, which is respectively weak in comparison with other velocity components. Graphics for OY axis velocity component show that the response comes to the receiver at the same time as the OZ axis velocity component response, and the signal has significantly less noise – a multiple response, the result of multiple elastic wave reflection, can be distinguished. With a small plate width (statement 5), the response merges with the beginning of the direct impulse, and the distance to the free border can be only defined by the multiply reflected waves frequency. Thus, the signals from separated-combined sensor (oriented across the fiber direction) become the most informative. Notice that Fig. 10 shows the dependency of signal in the receiver (velocity vector components) with a varying sensor size according to values from Table 1.

Graphics for all velocity components show that the direct wave signal length increases with the increasing sensor size, and its amplitude is decreasing. The response amplitude increases not only with respect to the direct wave, but also in its absolute value. The response amplitude is approximately twice as high as the direct wave amplitude in

statements 4 and 5. Similarly to the previous statements for monolayer, the most informative axis is the OY one, because OX and OZ axes components are noised. Thus, the usage of bigger sensors can decrease the demands on their sensitivity, but increase the size of the "blind zone" – a volume, which is located below the sensor near the front side of the plate, where the damages are indistinguishable by the NDT sensor due to interference of the response and direct waves signals.

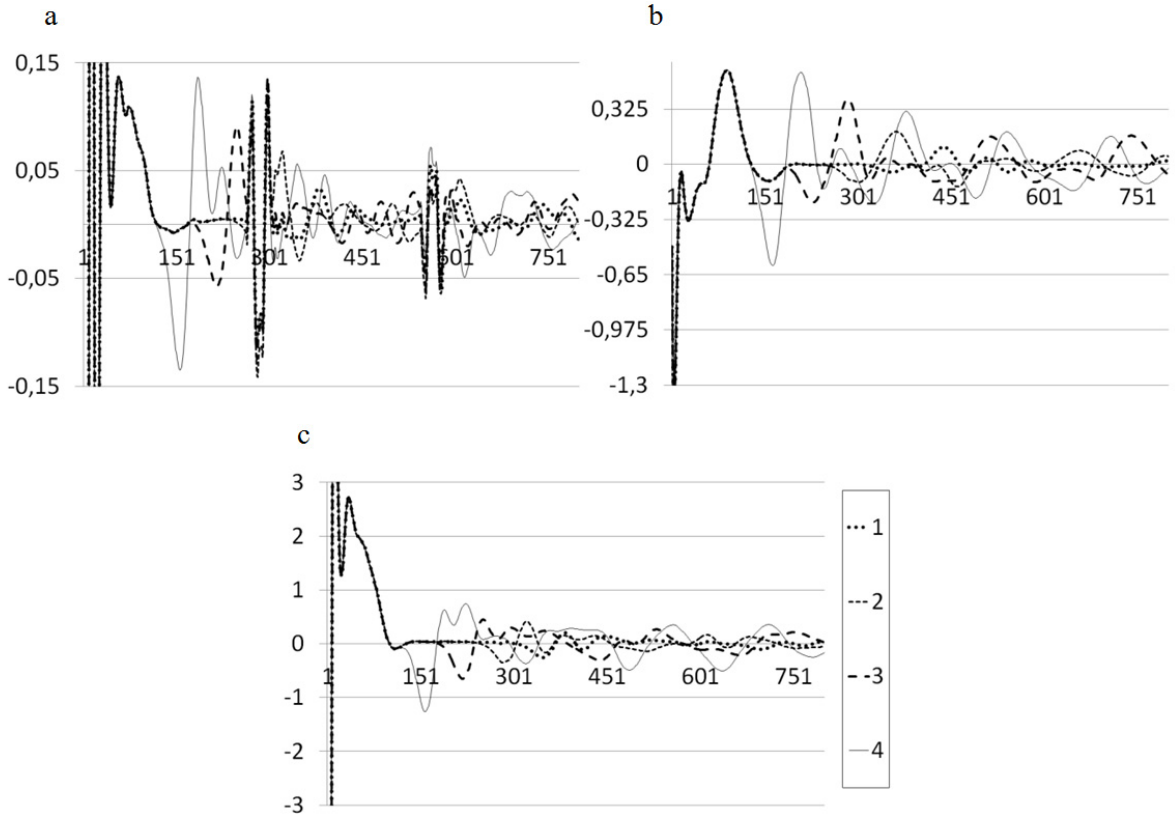

Fig. 10. Sensor data for a varying sensor size:(a) separated-combined sensor, oriented by x axis, v_x; (b) separated-combined sensor, oriented by y axis, v_y; (c) combined sensor, v_z. X axis – step number, y axis – velocity, m/s. Different line types correspond with statements from Table 1.

7. Conclusions

The wave pattern, appearing after a strike on an anisotropic plate surface, has a much more complex structure than in the case of isotropic material. Analysis of the dynamic wave pattern in various cuts can help to predict or interpret the processes of propagation, reflection, and refraction of wave fronts. Without signal processing algorithms, this analysis causes the difficulties in understanding. The isotropic and anisotropic materials were considered in this research. In the case of three or more anisotropic layers with different fiber directions, the wave pattern becomes too complex, and an immediate analysis of sensor data becomes impossible.

Analysis of numerical simulation data shows that in the case of isotropic material (metal) the most useful velocity component is the one along the OZ axis (perpendicular to the surface). This component is also the easiest to detect, and the existing NDT devices are oriented to work with it. In the case of anisotropic material (composite), it would have been more useful to measure a velocity component, parallel to the surface and perpendicular to the fiber direction, using separated-combined sensor.

In the current research, a carbon fiber epoxy matrix composite is modeled as a homogenous material with the averaged parameters. Contacts between fiber and matrix materials have a complex shape and a significant amount of

microscopic defects, and the difference between these material parameters is enough to increase wave dissipation and add noise to the sensor signal. An assessment of the amount of this noise and their elimination is necessary for the development of NDT devices, especially for the further mathematical modeling. Thereby, the current research can serve as a starting point for solving the composites NDT problem via mathematical modeling of occurring processes.

Acknowledgements

The work was supported by RFBR (grant 16-07-00884 A).

References

1. Hinton M.J., Kaddour A.S. Maturity of 3D failure criteria for fibre-reinforced composites: Comparison between theories and experiments: Part B of WWFE-II. *Journal of Composite Materials* 2013:**7**:925-966.
2. Hinton M.J., Kaddour A.S., Soden P.D. Failure criteria in fibre reinforced polymer composites: the world-wide failure exercise. *Amersterdam; London : Elsevier.* 2004.
3. Batra R.C., Gopinath G., Zheng J.Q. Damage and failure in low energy impact of fiber-reinforced polymeric composite laminates. *Composite Structures* 2012:**94(2)**:540–547.
4. Richardson, M. O. W., Wisheart, M. J. Review of low-velocity impact properties of composite materials. *Composites Part A-Applied Science and Manufacturing* 1996:**27(12)**:1123-1131.
5. Sjoblom P.O., Hartness J.T., Cordell, T.M. On low-velocity impact testing of composite materials. *J. Compos. Muter.* 1988:**22**:30-52
6. Cantwell, W.J., Morton, J. The impact resistance of composite materials. *Composites* 1991:**22(5)**:347-362.
7. Liu, D., Malvem, L.E. Matrix cracking in impacted glass/epoxy plates. *J. Compos. Mater*. 1987:**21**:594-609.
8. Raillon R., Toullelan G., Darmon M., Lonné S. "Experimental study for the validation of CIVA predictions in TOFD inspections", 10th International Conference on NDE, Cannes, France, 2013.
9. Duarte De Almeida P., Marcos Alcoforado Rebello J., Ribeiro Pereira G., Damasceno Soares S., Fernandez R. Ultrasonic Inspection of Adhesive Joints of Composite Pipelines. QNDE, Baltimore, USA, 2013.
10. Foucher F., Lonné S., Dominguez N., Mahaut S., Leymarie N. Contribution of numerical simulation to composite parts UT inspections. "Composite" seminar, 2012.
11. Abrate S. Criteria for yielding or failure of cellular materials. *Journal of Sandwich Structures and Materials* 2008:**10(1)**:5–51.
12. Hu, N., Zemba, Y., Okabe, T., Yan, C., Fukunaga, H., and Elmarakbi, A. A New Cohesive Model for Simulating Delamination Propagation in Composite Laminates under Transverse Loads. *Mechanics of Materials* 2008:**40(11)**:920-935.
13. Radchenko A, Radchenko P. Modelling of Fracture of Anisotropic Composite Materials Under Dynamic Loads. *Composites And Their Properties, edited by N. Hu. InTech, Croatia*. 2012:107-130.
14. Petrov I.B., Vasyukov A.V., Beklemysheva K.A., Ermakov A.S., Dzuba A.S., Golovan V.I. Chislennoye modelirovalie dynamicheskih processov pri nizkoskorostnom udare po kompozitnoy stringernoi paneli. Matematicheskoye modelirovanie 2014:**26(9)**:96-110.
15. Titov S.A., Mayev R.G, Bogachenkov A.N. Malogabaritnyi mnogokanalnyi skaniruyushyi akusticheskiyi microscop. *Probory I Tehnika experimenta* 2009:**5**:116-120.
16. Magomedov K.M., Kholodov A.S. Setochno-kharakteristicheskie chislenye metody. *M.: Nauka.* 1988.
17. Chelnokov F.B. Iavnoe predstavlenie setochno-kharakteristicheskikh skhem dlia uravenii uprugosti v dvumernom i trekhmernom prostranstvakh. *Matematicheskoe modelirovanie* 2006:**18(6)**:96-108.
18. Beklemysheva K.A., Danilov A.A., Petrov I.B., Vassilevsky Y.V., Vasyukov A.V. Virtual blunt injury of human thorax: Age-dependent response of vascular system. *Russian Journal Of Numerical Analysis And Mathematical Modelling* 2015:**30(5)**:259-268.
19. Petrov I.B., Kvasov I.E. High-performance computer simulation of wave processes in geological media in seismic exploration. *Computational Mathematics and Mathematical Physics* 2012:52(2):302-313.
20. Petrov I.B., Kvasov I.E., Pankratov S.A. Numerical simulation of seismic responses in multilayer geologic media by the grid-characteristic method. *Mathematical Models and Computer Simulations* 2011:**3(2)**:196-204.
21. Beklemysheva K.A., Petrov I.B., Favorskaya A.V. Numerical simulation of processes in solid deformable media in the presence of dynamic contacts using the grid-characteristic method. *Mathematical Models and Computer Simulations* 2014:**6(3)**:294-304.
22. Petrov I.B., Kvasov I.E, Golubev V.I. Influence of natural disasters on ground facilities. *Mathematical Models and Computer Simulations* 2012:**4(2)**:129-134.
23. Agapov P.I., Belotserkovskii O.M., Petrov I.B. Chislennoe modelirovanie posledstvii mekhanicheskogo vozdeistviia na mozg cheloveka pri cherepno-mozgovoi travme. *Zhurnal vychislitelnoi matematiki i matematicheskoi fiziki* 2006:**46(9)**:1711-1720.
24. Petrov I.B., Favorskaya A.V., Vasyukov A.V., Ermakov A.S., Beklemysheva K.A., Kazakov A.O., Novikov A.V. Numerical simulation of wave propagation in anisotropic media. *Doklady Mathematics* 2014:**90(3)**:778-780.